

Nanoscale and Microscale Thermophysical Engineering

ISSN: (Print) (Online) Journal homepage: https://www.tandfonline.com/loi/umte20

Optical Analysis and Optimization of Micropyramid Texture for Thermal Radiation Control

Jonathan Sullivan, Ziqi Yu & Jaeho Lee

To cite this article: Jonathan Sullivan, Ziqi Yu & Jaeho Lee (2021): Optical Analysis and Optimization of Micropyramid Texture for Thermal Radiation Control, Nanoscale and Microscale Thermophysical Engineering, DOI: <u>10.1080/15567265.2021.1958960</u>

To link to this article: https://doi.org/10.1080/15567265.2021.1958960

+	View supplementary material 🗗
	Pub l ished online: 02 Aug 2021.
	Submit your article to this journal 🗷
hil	Article views: 130
Q	View related articles 🗗
CrossMark	View Crossmark data ☑





Optical Analysis and Optimization of Micropyramid Texture for Thermal Radiation Control

Jonathan Sullivan, Ziqi Yu, and Jaeho Lee

Department of Mechanical and Aerospace Engineering, University of California Irvine, United States

ABSTRACT

While anti-reflective properties of pyramid texture are widely used, their use for thermal radiation control has received relatively little attention and the understanding of geometric parameters for design optimization is not well established. Here we use finite-difference time-domain simulations in conjunction with an algorithm to optimize thermal characteristics of micropyramid-textured metallic, ceramic, and polymer materials. Our simulations indicate that the pyramid height-to-base ratio is an effective parameter in developing an engineered thermal response. For nickel, the micropyramids with 2-4 height-to-base ratios over 0.5-4 µm base spans provide nearperfect absorption in 300-2500 nm wavelengths. The electric field analysis shows the optical properties are driven by the effects of localized resonance and field confinement. Our thermal cost function-based optimization has led to micropyramid texture that can have a significant impact on heating or cooling such as the solar absorption increase in nickel from 337 to 982 W/m², the thermal emission increase in alumina from 106 to 170 W/m², and the thermal emission increase in PDMS from 160 to 172 W/m². This work not only provides the understanding of micropyramid properties for thermal radiation control but also presents an algorithmic process that could be used for efficient optical-thermal optimization of geometries beyond micropyramids.

ARTICLE HISTORY

Received 16 March 2021 Accepted 16 July 2021

KEYWORDS

Thermal-optical optimization; micropyramids; selective absorber; passive cooling

Introduction

An approach that has proven to be effective in engineering surface optical properties is patterning a microscale pyramid-like ("micropyramid") surface texture into a material. The influence of periodic pyramidal design is well established in the field of optics as it is known to induce anti-reflective properties at the surface as a result of light confinement by the texturing [1] [2]. One of the most common applications of micropyramid texturing is in the design of "Black Silicon" - silicon that appears black due to a significant reduction in the optical reflectivity due to micropryamid structuring [3]. Micropyramid and nanopyramid patterned silicon designs have been widely adopted for solar cell applications as the pattern leads to enhanced photon absorption in the visible (VIS) and near-infrared (NIR) wavelengths [1] [4-7]. The design can be further enhanced with the inclusion of nanoscale hierarchy - either in the form of silicon nanopillars/wire architecture [8-9 21] or hybrid-material nanowires [10] [11]. Silicon micropyramids can also be coated with another material - adding an additional element of control over light interaction with the surface [12]. Micropyramid geometries have also been utilized to significantly enhance the solar absorptivity of metals. Micropyramids made of nickel have received attention for solar applications due to nickel's favorable mechanical/optical properties, with previous studies utilizing core-shell nanoscale nickel pyramids for thermophotovoltaic/Solar applications [13] or as a protective layer in solar panels [14]. Tungsten (W) pyramidal grating structures have also been explored for high-temperature absorption applications: with the geometry enhancing the metal's solar absorption coefficient to 0.92 [15]. The anti-reflective properties of micropyramid texturing has also been demonstrated to enhance the absorption characteristics of dielectric [2] and polymer [16] materials. Pyramidal surface features have broad appeal as they are both easily manufacturable and scalable [13] and can be patterned into a wide variety of materials via the template stripping technique [17] [18]. Further, pyramidal topology has demonstrated self-cleaning and hydrophobic properties [4], making it attractive for many applications.

For thermal radiation control applications, there are two spectral regions of interest for any surface: VIS/NIR and mid-infrared (MIR). The former is the most important optical parameter for solar applications as the spectral absorption from $\lambda=300$ –2500 nm determines the quantity of solar energy absorbed by the surface. While silicon micropyramids enhance absorption of visible light, beyond $\lambda=1000$ nm the drop in extinction coefficient and rise in transmission in Si [19] [20], leads to a decay in the pattern's absorption enhancement. As a result, the optical properties of Si micropyramids and nanostructuring have been studied extensively between $\lambda=400$ –1100 nm [4-8][21]. Use of coatings and fabricating micropyramids in other materials extends the region of efficacy and can also influence the NIR/MIR emissivity [13] [15], a key parameter in the determination of thermal emission from a surface. Micropyramids have been shown to enhance absorption in SiN between $\lambda=1$ –2.5 µm [22], inverse-Si micropyramids coated with Pt can increase emission between $\lambda=1.4$ –5 µm [23], and advanced processing can result in enhanced absorption through the MIR [24]. Already MIR emissive materials – such as polymers [16] and SiO₂/HfO₂ [25] – can have near perfect emission in the infrared when patterned with micropyramids.

Control over the spectral absorption and emission properties of a material can yield unique thermal solutions. Beyond micropyramids, other surface topologies such as nano-domes [26], corrugated surfaces [27], and core-shell structures [28], and gratings [29] have been proposed for high-efficiency solar absorption. By enhancing the spectral emissivity in the infrared region, surfaces can leverage the sky-transparency window to emit radiation to space and cool beneath ambient temperatures [30]. Referred to as "passive radiative cooling," solutions range from corrugated graphene/nickel structures [31] [32], to multilayer stacks [33], and engineered polymers [34-35][40]. Solutions for both radiative heating and cooling demonstrate wide-variation in design, but a common difficulty is engineering scalability, cost-effectiveness, and limited applications of the materials utilized. Micropyramid structures offer a simple and scalable design that can be patterned into a vast range of materials, allowing for a large design space.

In the present study, we study the fundamental relationship between micropyramid geometry and thermal radiation control. As shown in Figure 1, by utilizing the spectrally dependent anti-reflective behavior induced by pyramidal topology [36], we can significantly enhance the thermal absorption of metallic surfaces and the thermal emission of ceramic and polymer surfaces We develop and utilize a generalized framework that combines thermal cost-function driven design optimization with finitedifference time-domain simulations to provide design criteria for micropyramid texturing that enhances the heating or cooling performance. This is a far simpler optimization approach compared to more advanced techniques used previously for optical/thermal optimization, including machine learning models and deep-neural networks [29] [37-39]. As a result, the method is easy to implement and replicate for any number of domain variables or geometries, requiring no existing training data or advanced processes. In this study, nickel is selected as the basis for the heating material optimization due to its favorable material properties that enable its usage in solar absorption and high-temperature applications such as for thermophotovoltaics (TPVs), solar thermal power plants, solar water heaters, etc. For passive radiation cooling applications, we establish that introducing pyramidal topology further enhances the MIR emissivity of Polydimethylsiloxane (PDMS) and Alumina (Al₂O₃) surfaces. Both materials have a refractive index that generates emission in the IR spectrum, which enables excellent passive cooling performance. PDMS is chosen due to the manufacturing processing being low-cost and scalable, ceramic materials are far more environmentally adaptable, allowing for reliable radiative cooling over a wide range of operating temperatures. While we show results primarily for

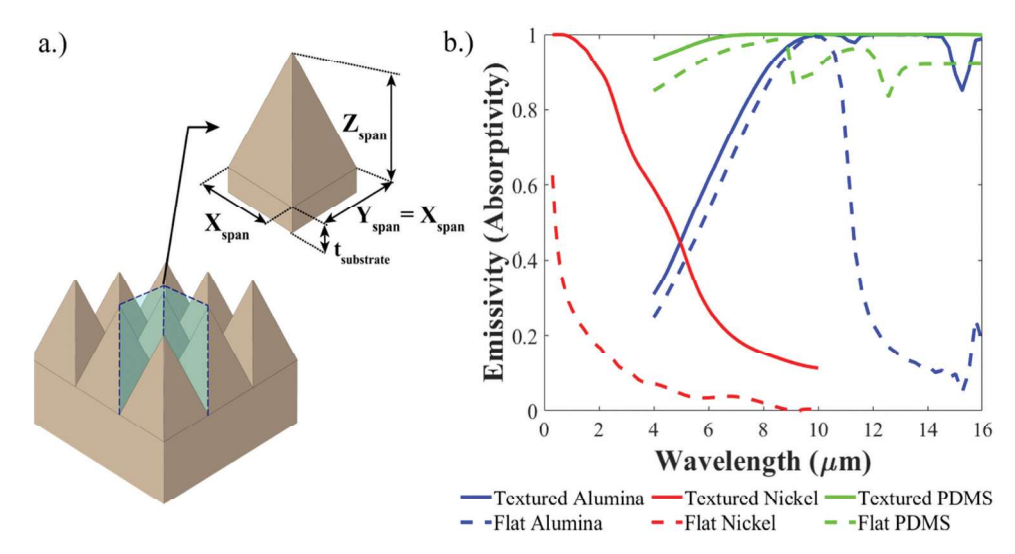


Figure 1. (a) Micropyramid geometry utilized in simulation. The blue region represents the imposed periodic boundary conditions, with the pyramid cutout being the simulated unit cell. The 3-D unit geometry shown is extended infinitely in the X and Y directions. The z_{span} and x_{span} vary from 50 nm to 30 µm in simulations, and the y_{span} is set to be symmetric with the x_{span}. The substrate thickness is established per material to limit the impact of transmission - 1 um for nickel and 100 um for Alumina and PDMS simulations. (b) The emissivity of both optimized and flat nickel, alumina, and PDMS. The optimized nickel ($z_{span}/x_{span} = 2.1/0.6 \mu m$) result has a strong dependence on aspect ratio, the PDMS and alumina optimized cases $(z_{span}/x_{span}=15/5~\mu m$ and $z_{span}/x_{span}=16/5~\mu m$ 6 µm, respectively) also show strong dependence on aspect ratio for the enhancement of emission properties in the IR.

these three materials, the design criteria and physical insight presented from these materials can be used to extrapolate generalized design rules for other similar metallic, ceramic, and polymer materials.

Methods

A generalized simulated unit cell is visualized geometry shown in Figure 1(a) and a flowchart depicting the optimization and simulation process is shown in Figure 2(a). Beginning with a depiction of intent of the surface material - either to absorb solar radiation or for thermal emission Figure 2(b) a minimization cost function is defined. The objective (or cost) function serves as a mathematical quantification of a design's thermal performance for the chosen application. For both heating and cooling applications, the cost function has been designed such that in the ideal scenario the constituent thermal terms cancel, and the objective function value becomes 0, lending to the minimization process. In the instance of heating, the primary thermal goal is to minimize the amount of heat lost in the IR while maximizing the amount of incident radiation absorbed [13]. We define the objective function for this scenario to be generally defined by the heat transfer balance of,

$$C_{heating} = \frac{P_{sun} - P_{abs} + P_{rad}}{P_{sun}} \tag{1}$$

Cheating =
$$\frac{\lambda_{max}}{\int_{Miin}^{\lambda_{max}} I_{AM1.5}(\lambda) d\lambda} - \int_{\lambda_{miin}}^{\lambda_{max}} \varepsilon(\lambda) I_{AM1.5}(\lambda) d\lambda + \int_{\lambda_{min}}^{\lambda_{max}} \varepsilon(\lambda) I_{BB}(\lambda, T) d\lambda$$

$$\frac{\lambda_{max}}{\int_{\lambda_{min}}^{\lambda_{max}} I_{AM1.5}(\lambda) d\lambda}$$
(2)

Where $I_{AM1.5}$ is defined as the solar irradiance for an airmass value of 1.5, I_{BB} is the spectral radiance for a blackbody, and $\varepsilon(\lambda)$ is the spectral emissivity of the surface. The first term is the maximum

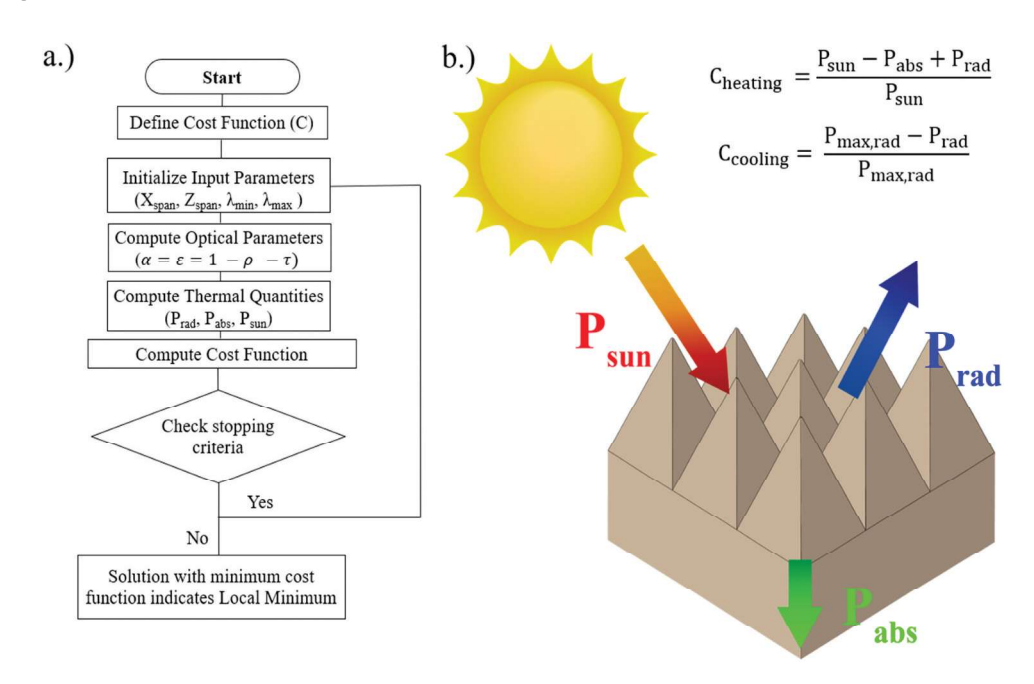


Figure 2. (a) Flowchart showing the optimization methodology. Gradient descent optimization tools within MATLAB are linked to FDTD simulations to optimize optical properties for intended thermal performance based on a chosen cost function (Cheating or Cooling). (b) Cost functions visualized with a heat-flow system diagram. The convection/conduction contribution (Pconv+cond) and atmospheric contribution (Patm) are not utilized in the present study.

amount of power that is available for the surface to absorb. For the majority of applications solar irradiation is dominant, so we define the maximum amount of power available to be a function of the solar spectrum. This term is independent of material parameters and can be treated as a constant heat flux. The second and third terms are the amount of incident radiation that is absorbed by the surface and the amount of power emitted by the surface, respectively. Atmospheric contributions are neglected in the cost-functions utilized in this work. Atmospheric contributions are relevant for thermal temperature estimations – particularly for passive cooling [33] – but is significantly smaller than the thermal emission and thermal absorption so we **choose** to not include it in the cost functions. It can be accounted for, however, by including an additional thermal offset term like the emitted radiation term in Equation 1. We also do not include the effects of thermal convection/conduction as the surface emissivity does not impact the heat flux from convection and conduction. The entire cost function is normalized by the maximum power available yielding a value for the cost function that is between 0 and 1. Before normalization, the equation has the unit of area independent power, W/m².

The cost function used in the optimization of radiative cooling surfaces minimizes energy absorbed while maximizing emission. We define the objective function in a similar fashion to the heating case with the heat transfer balance,

$$C_{cooling} = \frac{P_{max, rad} - P_{rad}}{P_{max, rad}} \tag{3}$$

$$C_{cooling} = \frac{\int_{\lambda_{min}}^{\lambda_{max}} I_{BB}(\lambda, T) d\lambda - \int_{\lambda_{min}}^{\lambda_{max}} \varepsilon(\lambda) I_{BB}(\lambda, T) d\lambda}{\int_{\lambda_{min}}^{\lambda_{max}} I_{BB}(\lambda) d\lambda}$$
(4)

While there is some small amount of absorption in the optical wavelengths by emissive materials (PDMS and alumina in this case), it is small enough that we can omit it from the heat transfer balance shown in Equation 3. Similarly, we do not include the effects of atmospheric emission in the heat

balance equation to maintain a simple relationship between the maximum emission and achieved emission by the surface in the optimization process. The Heat-flux computations shown for both the heating and cooling cases are computed using a blackbody temperature of 300 K. For the thermal absorption estimations of flat/textured nickel, the value presented is P_{abs} at a I_{BB} Temperature of 300 K between $\lambda = 300$ nm to 2500 nm. Similarly, the thermal emission fluxes (P_{rad}) of alumina and PDMS are computed between $\lambda = 8 \ \mu m$ to 14 μm at $I_{BB}(T) = 300 \ K$.

For a micropyramid texture like the depiction in Figure 1(a), only two parameters (x_{span} and z_{span}) are optimized but the method can accommodate many more design variables. The design parameters (x_{span}) and z_{span} are defined and passed to the simulation domain for each iteration. The simulation domain utilized in the simulation and optimization process is depicted in Figure 1(a). The illustration demonstrates both the periodicity of the design and the details of the 3D pyramidal unit cell simulated. The key geometric parameters of the unit cell are specified by the span of the pyramid's base and its height (x_{span} and z_{span} respectively). We only consider the case where the structure's base is symmetric, so x_{span} is equal to the span along the y-axis (y_{span}). The "gap" distance between the edges of adjacent pyramids - which would be a consequence of typical fabrication techniques for periodic microstructures – is not considered in this analysis. The substrate thickness (t_{sub}) is set such that transmission through the simulation domain is negligible and thus this value varies with the chosen material.

The numerical simulations in our work are conducted using Lumerical's commercially available 2D/3D FDTD solver using a similar methodology shown in previous studies performed by the authors [31, 32, 40, 41] The FDTD method discretizes a volume via a mesh and provides exact 3D solutions for Maxwell's equations, including dispersion and absorption [42] [43]. We utilize the unit cell depicted in Figure 1(a) in conjunction with periodic boundary conditions in both the x and y-directions to simulate a semi-infinite surface microstructure on the x-y plane. Perfectly matched layers (PML) are used at the top and bottom of the simulation domain to prevent boundary reflection. A plane wave source is used for both normal incidence (polar angle, θ) and angular incidence simulations, but in the case of an angular injection angle, Broadband Fixed Angle Source Technique (BFAST)/Bloch periodic boundary conditions replace the periodic boundary conditions. Our plane wave source utilizes a transverse-electric (TE) polarization mode for all simulations, and we set the source angle to be 0° in both rotational directions for all simulations except for the results shown in Supplementary Figure 5. Frequency-domain field and power monitors are positioned both above the plane wave source and above the bottom PML to monitor the reflection (R) and transmission (T), respectively. The structure's spectral emission can be calculated from $\varepsilon = 1 - R - T$, assuming Kirchhoff's law $(\alpha = \varepsilon)$ is valid. For completely opaque structures, the computation of emissivity reduces to $\varepsilon = 1 - R$, but due to the negligible extinction coefficient (k) of both alumina and PDMS within the visible and NIR regions, we use both R and T in the calculation of spectral emissivity. We have validated our computational methodology by comparing the results to previous micropyramid studies [4, 13, 15].

The output of the simulation – $\varepsilon(x_{span}, z_{span}, \lambda)$ – is then used to compute and evaluate the objective (cost) function. This process begins with an initial guess for x_{span} and z_{span} ($x_{initial}$) upon which a baseline value for the cost function is calculated. The minimization function will then check the cost function when the values for x_{span} and z_{span} are varying combinations of above and below x_{initial} and z_{initial}. The range of either parameter is widely geometrically constrained depending on the material. Subsequent iterations will continue to test variations of x_{span} and z_{span} until the stopping criteria is reached; this value is based on a predefined error limit. The "optimum" value is the local minimum of the cost function for the combined array of x_{span} and z_{span}. MATLAB's gradient-descentbased optimization framework is used in conjunction with the FDTD simulation domain. Parametrically driven geometric parameters are also used to fill in grid data for the contour plots shown in Figures 3,5,7. Only two parameters (x_{span} and z_{span}) are optimized in the process shown in this work but the method can accommodate many more variables at the cost of additional computational time required to handle a larger design space. The results of the optimization process are visualized in Figure 1(b) – a micropyramid with an optimum x_{span} and z_{span} results in nickel becoming

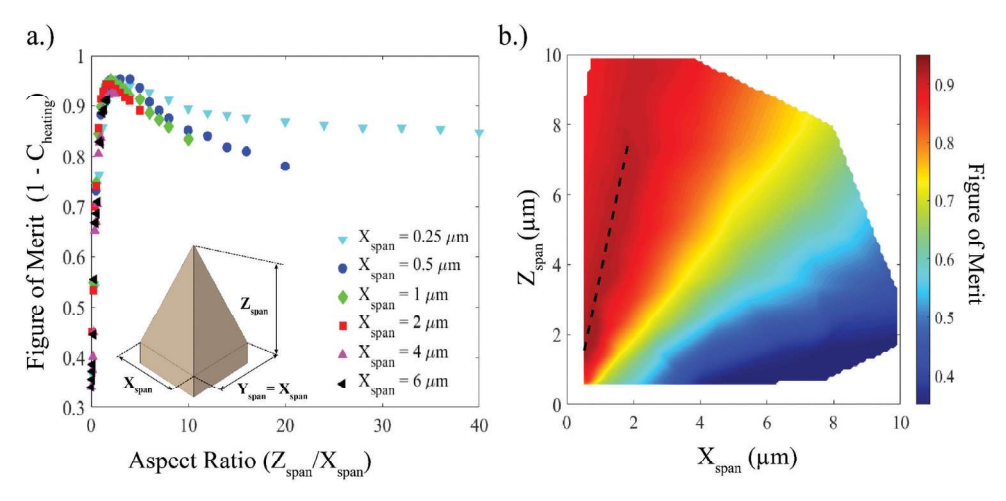


Figure 3. (a) The relation between the normalized aspect ratio and figure of merit plotted for the nickel texture with three different fixed base dimensions ($x_{span} = 0.25$, 0.5, 1, 2, 4, and 6 µm). In this plot, z_{span} is swept while x_{span} is held constant. (b) Contour plot of algorithmically derived solutions over a range of x_{span} and z_{span} combinations. Over 1500 solutions obtained from optimizations with different initialization points are used. Data interpolation is used to fill the remaining grid data. Among many FOM > 0.9 solutions an optimal region emerges as visualized by the dark-red region in the bottom left corner and along the dashed-black line.

a strong thermal absorber and micropyramids significantly enhancing the thermal emission of alumina and PDMS.

Results

Optimization of Nickel micropyramids

The combined results of the nickel micropyramid optimization process are shown in Figure 3(b)a. The minimization process relies on a gradient descent interior-point optimization algorithm [44] that optimizes the x span ($x_{\rm span}$) and z span ($z_{\rm span}$) of the pyramidal geometry (represented in Figure 1(a)) by minimizing a cost function defined by Equations 1 and 2, where $P_{\rm solar}$ is defined as the maximum amount of solar irradiation available to be absorbed, $P_{\rm abs}$ is the amount of thermal energy absorbed by the surface, and $P_{\rm rad}$ is the amount of lost to emission by the surface. Both $P_{\rm abs}$ and $P_{\rm rad}$ are functions of the surface emissivity computed within FDTD simulations. The cost function is normalized by the maximum available power such that 0 < C < 1. For the sake of visualization, we present the optimization results using a normalized figure of merit (FOM) defined by Equation 5, such that a value close to one indicates an optimal solution.

$$FOM = 1 - C_{heating} \tag{5}$$

For the nickel optimization process, we utilize a plane wave source of normal incidence in the FDTD simulations that ranges from 300 nm – 10 μ m. We choose this wavelength (λ) span as λ = 300–2000 nm is the most relevant region for solar absorption, and due to the high refractive index in the IR, nickel is observed to asymptotically approach an emissivity \sim 0.1–0.2 beyond λ = 10 μ m for most nickel micropyramid x_{span} and z_{span} dimensions. Figure 3(b) shows a contour map of geometric designs that result from numerous iterations of the minimization process for nickel when the cost function described by equation (5) is employed. To provide a reference point, untextured nickel – simulated as an untextured 1 μ m thick nickel substrate in FDTD – has a computed FOM of \sim 0.35. This is a result of the untextured nickel substrate absorbing nearly 37% of incident solar irradiation while only losing a fractional quantity of thermal power to emission in the IR due to low IR emissivity. Comparatively, Figure 3(b) demonstrates that even un-optimized surface structuring via

micropyramids drastically increases the FOM to 0.6-0.7, which is equivalent to a solar absorption efficiency of 60–70%, representing a 25–35% increase compared to bare nickel.

In Figure 3(b), the plotted contours show that the minimization process yields a host of solutions that are quintessentially optimal and have nearly negligible variation in optical performance. The maximum figure of merit computed from multiple iterations of the optimization process using Eq. 1 as the cost-function is 0.963, which occurs at $x_{span} = 0.65 \mu m$ and $z_{span} = 2.1 \mu m$. Both the emissivity and reflectivity of this structure can be observed in Figure 4(b), but the exceptional increase of absorptivity to a value near $\alpha = 1$ between the wavelengths of 300–2000 nm results in an absorption efficiency of 98.6%. Specifically, this structure can be predicted to absorb 986.6 W out of the available 1000.4 W for AM1.5 per square meter between $\lambda = 300$ nm and $\lambda = 10$ µm. Thermal emission leads to a thermal loss of 23.9 W/m² for the optimized structure, which is 19.1% of the maximum blackbody emission between $\lambda = 300$ nm and $\lambda = 10$ µm at 300 K. By comparison, two local minima occurring at $(x_{span} \times$ z_{span}) of (0.51 \times 1.45) μm and (0.9 \times 1.98) μm have absorption efficiencies of 97.3% and 96.9%, respectively. Accordingly, their FOMs are computed as 0.96 and 0.953. Although the absorption efficiency decreases by ~1-1.5% for both local optimums when compared to the best local minimum, a decrease in thermal emission - 13.8% and 13.7% of the blackbody limit, respectively - results in the best local minimum having a FOM that is only 0.3-1% higher than other local optimum geometries. Thus, while finding a global optimum using our gradient-descent-based optimization would be inefficient compared to methods such as particle swarm optimization [45] or genetic algorithms [46], finding a local minimum that has exceptional performance occurs very early in our process and we can reliably and rapidly reach designs that achieve absorption efficiencies exceeding 94-96%.

The overall trend in the heating FOM can thus be described predominantly as a function of the aspect ratio of the structure. This trend can be observed in Figure 3(a), which plots the FOM as

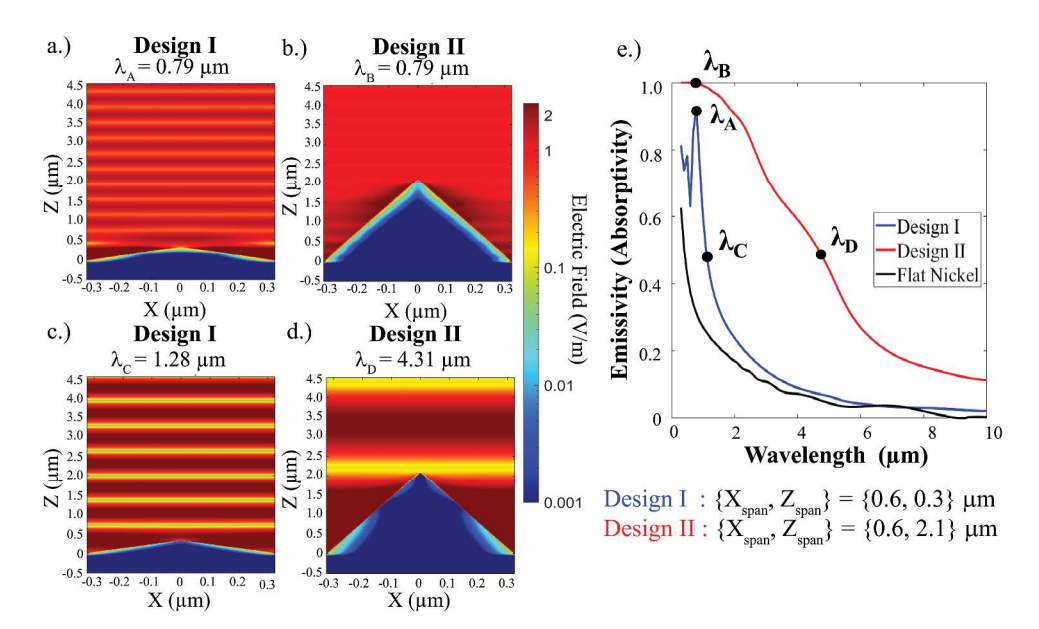


Figure 4. (a-d) Plots of the x-z plane (cross-sectional) Electric field (V/m) demonstrate that the optimized structure (Design II) more thoroughly confines the electric field within the texture, significantly enhancing the solar absorptivity. (a,b) At wavelength A and B (0.79 µm), where the emissivity of Design I reaches a peak – strong electric field confinement is observed in both structures. (c, d) At wavelength C and D, the effect of texture is apparent. The confinement of the electric field by Design II leads to Design II having an emissivity of 0.5 at $\lambda_D = 4.31 \,\mu m$ while Design I has an emissivity of 0.5 at $\lambda_C = 1.28 \,\mu m$. The higher aspect ratio Design II leads to a much slower decay in emissivity than with Design I. A log-scale is used to show the absorption more thoroughly in (a-d). (e) The emissivity of both Design I (low-aspect ratio) and Design II (optimized) structures are shown compared to the untextured case (Black), with the reflectivity of either structure visualized by the dashed lines.

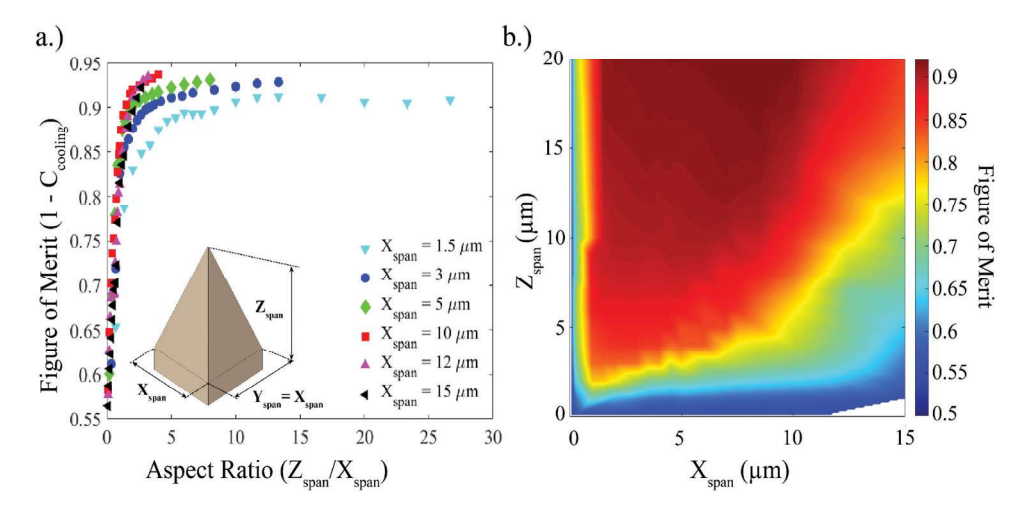


Figure 5. (a) The relation between the normalized aspect ratio and figure of merit plotted for six fixed base dimensions ($x_{span} = 1.5$, 3, 5,10, 12, and 15 μ m). (a) Contour plot of algorithmically derived solutions over a range of X and Z span combinations. Over 1300 solutions resulting from many optimization runs with different initialization points are plotted. Data interpolation is used to fill the remaining grid contours. The Optimal region can be identified from $x_{span} \sim 5-8 \mu m$ and $z_{span} \sim 15-20$ (b) The relation between the normalized aspect ratio and figure of merit plotted for six fixed base dimensions ($x_{span} = 1.5$, 3, 5,10, 12, and 15 μ m).

a function of the aspect ratio. It is important to note that while the aspect ratio is intrinsically unitless, we choose to define aspect ratio (AR) as:

$$Aspect \ Ratio = AR = \frac{Z_{span}}{X_{base}} \tag{6}$$

where x_{base} is constant and used to normalize while z_{span} is swept in the simulations. While we observe a trend between the aspect ratio and FOM, this distinction is made such that the necessity of a nanometer/micrometer scale periodicity on the absorption enhancement and anti-reflective properties is not lost. From Figure 3(a) we conclude that, based on a x_{base} from 500 nm to 2 μ m, increasing x_{span} will rapidly increase the FOM until it reaches a maximal value ~ 0.92 –0.96 for an aspect ratio of \sim 2 – 4. After the local maximum for a x_{base} , the FOM will then decrease. This trend can be explained as a function of both the thermal and absorption efficiency increasing until a critical maximum when the absorption efficiency saturates while the thermal emission efficiency continues to increase. At larger ARs, the absorption efficiency decreases while the thermal emission efficiency continues to increase.

The surface optical properties result from the introduction of anti-reflective behavior because of the patterned periodic structure as visualized in Figure 4(a-d). Two geometries are plotted in Figure 4(a-d) – Design I (a,c) and Design II (b,d). Design II is the optimized geometry for the nickel heating cost function, and Design I is a low-aspect ratio (AR = 0.5) structure. For comparison, both designs have the same $x_{\rm span}$ (0.65 µm). As the simulation domain has a near-zero transmission due to the intrinsically high extinction coefficient, the driving factor behind the emissivity/absorptivity enhancement is the decrease in reflection as a function of the geometry. As seen in Figure 4(a), the maximum intensity of electric field for the same wavelength remains contained in the optimized geometry and unconfined by the low-AR structure. The evolution in the magnitude of the normal electric and magnetic fields (E,H) with respect to wavelength is visualized in movie form in Supplementary Figure 1 for both the optimal and fixed AR geometries. It is evident that the higher AR structure maintains confinement – and increased absorption – over a much wider wavelength region compared to the low AR micropyramid texturing. It should be noted that based on Supplementary Figure 3 the magnetic field component plays a limited role in the enhancement of the absorption compared to the electric field.

While the results shown in Figure 3 occur using a three-dimensional (3D) FDTD design space, our optimization process readily transfers to a two-dimensional (2D) design space. Reducing the geometry to 2D yields a grating structure as the simulation domain assumes the triangular shape (x_{span}) and z_{span}) is infinitely extruded along the y-axis. For a plane wave with an injection angle of $\theta = 0^{\circ}$, there are minimal differences in the absorptivity computed between the 2D and 3D domains. The computed spectral emissivity of two optimal nickel geometries are plotted in Supplementary Figure 4 for different plane wave source incident angles (θ). A key difference between 2D and 3D simulations, however, can be seen in Supplementary Figure 5 where the 3D pyramidal geometry has near omni-directional absorption properties that are not observed in a 2D grating structure that has been extruded into three-dimensions. While a 2D cross-section provides an excellent estimation of the 3D micropyramid's optical properties, there is a slight overestimation of the emissivity for this structure. When the 2D structure is simulated with a third dimension, the results of the grating structure geometry vary greatly from the pyramidal geometry. This discrepancy is most apparent at different angles, as the pyramidal geometry demonstrates consistently omnidirectional properties.

Optimization of alumina and PDMS micropyramids

The results of the alumina and PDMS micropyramid optimization processes are shown in Figure 5 and Figure 7, respectively. Similar to the nickel optimization, the optimization occurs by minimizing a cost function that is defined by Equation 3 and 4. where P_{max,rad} is defined as the maximum amount of thermal emission that is possible according to Planck's law [47], and P_{rad} is the thermal energy emitted by the surface. P_{rad} is a function of the surface emissivity computed within FDTD simulations. For these thermal calculations, we define the surface emission temperature to be 300 K. The FOM presented in Figures 5–7 is defined by equation (6). For both the alumina and PDMS optimizations, we apply a plane wave source that ranges from $4 \mu m - 16 \mu m$. This wavelength span is utilized because the blackbody distribution for a body at 300 K centers near ~10 µm, with over 60% of the total thermal emission possible occurring in this span. Simultaneously, both materials are highly transmissive in the Vis/NIR region for the thickness required by the simulation to negate MIR transmission (100 μm). Consequently, the VIS/NIR response of the cooling materials is not a function of geometric optimization and is instead a function of the substrate.

The contour plot of solutions visualized in Figure 5(b) demonstrates that a large range of geometric combinations for alumina yields highly optimal results. The results in Figure 5(a) for FOM vs. Fixed-Base AR also establish that the FOM of the ceramic texture has a strong dependence upon x_{span} . For the results shown in Figure 5(a), the z_{span} is limited to 40 μm . Based on the results shown in Figure 5(a, b), however, the near equivalency in thermal emission between structures with AR > 2-5 mitigates the necessity of simulating structures beyond this constraint. The trend in the FOM is to asymptotically approach a maximum that is dependent upon x_{span} for the structure. When $x_{span} = 10$ µm, the FOM approaches ~ 0.95, indicating that the geometry can emit ~95% of the theoretical maximum at 300 K. Comparing $z_{span} = 5 \mu m$, $10 \mu m$, $20 \mu m$, and $40 \mu m$ for a fixed z_{span} of $10 \mu m$, the FOM is 0.753, 0.856, 0.920, and 0.937, respectively (AR = 0.5, 1, 2, 4). This corresponds to an increase in FOM of \sim 0.22, 0.32, 0.39, and 0.41 when compared to bare alumina. The asymptotic behavior between AR and FOM indicates that while the maximum for a given z_{span} might not be observed when the z_{span} is constrained, increasing z_{span} will not significantly impact the FOM. The optimization of the cooling cost function for alumina quickly yields local minima beneath $C_{cooling} = 0.1$ (FOM = 0.9) but this solution is unlikely to contain the entirety of the optimal geometric region due to the constraints utilized.

The negligible difference between the cost functions at higher ARs is a result of a saturation in emissivity. The results plotted in Figure 6(e) show that the micropyramid pattern significantly reduces reflection that occurs in the MIR beyond $\lambda = 10 \mu m$. The anti-reflective behavior can again be observed in Figure 6(a-d) to be a function of the confinement of the electric field by the geometry. While the efficiency of the anti-reflective behavior is a function of the geometry, the emissivity can only range

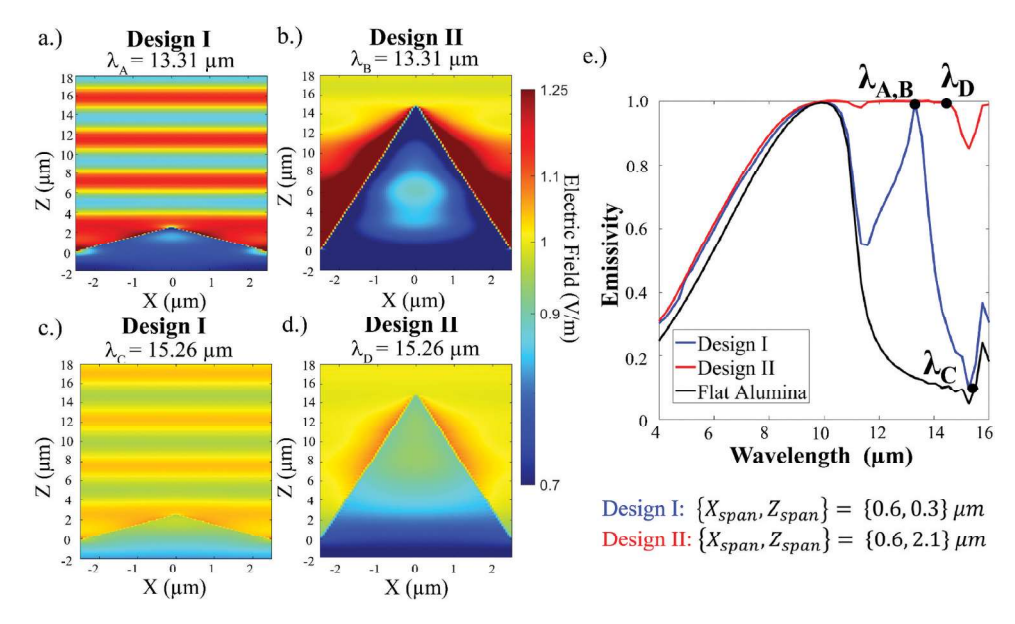


Figure 6. (a) Electric field cross-sections for alumina that demonstrate that the optimized structure (Design I) more thoroughly confines the electric field inside the texture, significantly enhancing the solar absorptivity. Wavelength A (13.06 μ m), where the emissivity of Design I is maximal – and wavelength B (15.26 μ m), where the emissivity of Design II reaches a minimum. A log-scale is used to show the absorption more thoroughly within the micropyramid at both points. (b) The emissivity of both Design I (optimized) and Design II (low aspect ratio) structures are shown compared to the untextured alumina case (Black), with the reflectivity of either structure visualized by the dashed lines.

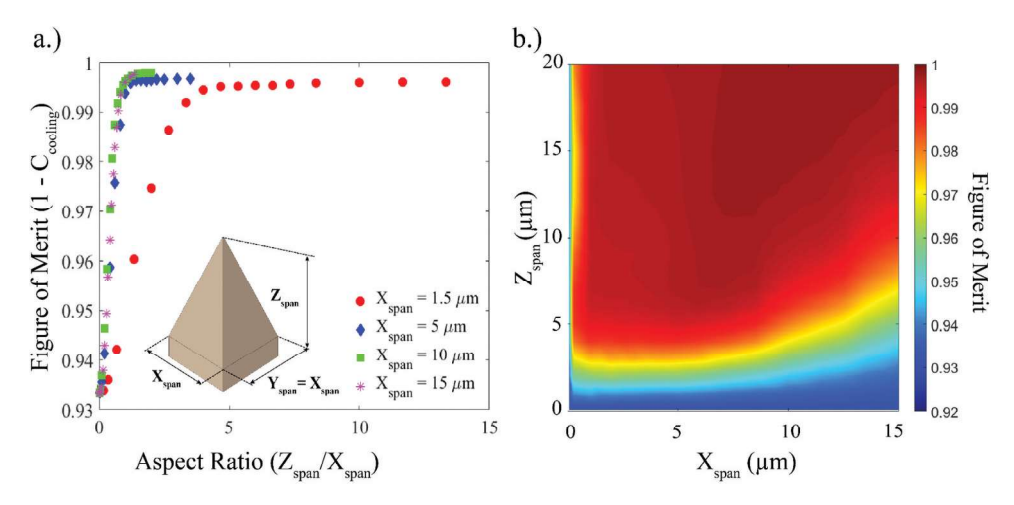


Figure 7. (a) The relation between the normalized aspect ratio and figure of merit plotted for four fixed base dimensions ($x_{span} = 1.5$, 5,10, and 15 μ m). The relation between the aspect ratio and figure of merit is shown to asymptotically approach 1. Higher aspect ratio structures are shown to approach higher values for FOM, but with larger base dimensions, the necessity of high aspect ratio structures is minimized as the structure's emission reaches a maximal point and the aspect ratio no longer influences the optical properties. (b) Contour-plot of algorithmically derived solutions over a range of X and Z span combinations for PDMS. Similar to alumina, identifying the bounds of the optimal region for the PDMS texture is more challenging as a result of the geometric scale and time required to simulate larger structures.

from 0 to 1, so the influence of geometry on the emissivity decreases both as the AR increases and X_{span} increases. This phenomenon is seen in Figure 6(e), in which a low-AR (0.5) and high-AR (3.0) geometry are plotted simultaneously. Compared to the bare alumina case, the low-AR micropyramid pattern has a drastic effect on the emissivity by significantly decreasing the spectral reflectivity when $\lambda > 10 \, \mu m$. For the high-AR geometry, the emissivity is almost a unity across the spectrum, leaving marginal room to further improve the emissivity.

Although PDMS has an innately high emissivity in the MIR/NIR regions due to its intrinsic refractive index [48], employing the same cooling optimization procedure results in the same antireflective trend and subsequent increase in MIR emission that has been observed in alumina. The cooling cost function equation defined by Equation 3 and 4 that was used for the alumina optimization results in a FOM = 0.91 ($C_{cooling} = 0.09$) for untextured PDMS. The results shown in Figure 7(b) exemplify that even minor texturing of a PDMS surface can increase the FOM to a value near 1.0, indicating that textured PDMS is a near perfect NIR/MIR emitter when textured. Despite having a characteristically high emissivity, the introduction of micropyramid texture to the surface reduces the already minimal reflectivity to a value near 0 in the NIR/MIR. The trend observed in Figure 7(a) is that even low-AR texturing with AR < 1 yields emission efficiencies of 95-96%, with AR > 2 PDMS micropyramids displaying thermal emission efficiencies of ~99% or higher for pyramidal base dimensions near the IR wavelength.

Discussion

Planar metallic surfaces are generally poorly absorbing materials – this is due to most metals being conductive and thus featuring a steep complex refractive index curve that leads to untextured metals being highly reflective. Although the characteristically high reflectivity of metals can be reduced by introducing severe oxidation at the surface, we have demonstrated that strong absorption within the visible and NIR regions is possible by microscale geometric patterning of a nickel surface without the need for an oxide coating or nanoscale texturing. The relation between the absorptivity enhancement and geometry of the texturing is fundamentally linked via the material's refractive index. For nickel, the refractive index in the VIS/NIR enables strong geometrically based anti-reflective behavior. Thus, nickel is very well suited to optimization as a passive radiative heating material. Subsequently, the goal of the optimization process for nickel is to maximize the amount of energy absorbed - particularly in solar relevant wavelength regime of 500-1000 nm - while minimizing the amount of energy lost to emission. While further emissivity enhancement is possible geometrically beyond the NIR, this is counter-productive to the goal of minimizing energy loss via emission. If the optimization intent is high temperature cooling instead of solar absorption, then the increased importance of MIR/NIR emissivity to the spectral distribution would necessitate higher emissivity texturing for λ beyond 3-4 μm. While we do not demonstrate a metallic high temperature cooling optimization procedure in this work, this form of optimization is easily performed with our method by adjusting the cost function equation and the emission temperature.

The absorption enhancement provided by the nickel texturing in the VIS/NIR is a combined effect of the complex refractive index and the geometric scale of the nickel micro/nanopyramidal surface topology. For wavelengths beyond the solar spectrum (> 2000–3000 nm) the complex refractive index of nickel begins to rapidly rise, which leads to surface morphology having a reduced impact on the optical properties of the surface. Figure 3(a) validates that while increasing the AR to form very steeply angled structures (AR > 5) can lead to a moderately increased absorption coefficient in the IR-band, it is far more limited in scope than the geometric enhancement available in the visible/NIR. From simulations with other metals such as silver and aluminum shown in Supplementary Figure 6 we observe that geometric-dependent anti-reflective behavior has a far more limited spectral range of influence. This is predominantly due to a much higher slope in the refractive index for these materials that limits the spectral enhancement provided by surface geometry. Additionally, the optimization



process yields that the most optimal results have $x_{\rm span}$ comparable to solar spectrum wavelengths ($x_{\rm span}$ $\sim 500\text{--}2000$ nm for $\lambda_{solar} \sim 300$ nm – 2400 nm).

The results shown are for nickel, alumina, and PDMS are to be expected as localization and resonance effects as a function of geometry are most effective when the structure's period dimension is sub-wavelength [49]. Micropyramid textures are also known in the broader community as a surfacerelief gratings or anti-reflection gratings (ARGs). When the incident wavelength is much larger than the critical dimensions (Λ) of the ARG, or $\lambda \square \Lambda$, the electromagnetic propagation through the structure can be approximated via an effective-medium electric permittivity function that has a gradient in the z-direction [1] [2]. The interaction of light with sub-wavelength structures (SWS) can also be approximated by Maxwell-Garnett (MG) [50, 51] or Bruggeman [52] effective-medium theory (EMT) models. Both of these EMT approximations represent the heterogeneity of a ARG in terms of a homogeneous medium with a single effective complex refractive index [49].

For our micropyramid-based ARG topology, as the complex refractive index in the IR (where λ Λ , for small x_{span} nickel textures) is large, the structure behaves much like untextured nickel, with a high reflectivity. In the case where $\lambda \Box \Lambda$, the structure can be visualized using geometric optics, with light potentially being preferentially confined by the geometry due to the multiple scattering interfaces induced by the texture [1] [2]. While increasing x_{span} to being comparable to IR wavelengths does have the expected effect of slightly increasing emission properties in the IR, it also causes the solar absorption properties to be significantly reduced. This effect can be visualized in Figure 3(a), where pyramids featuring a larger base dimension also have a reduced figure of merit due to the reduced inability to absorb incident solar radiation in the visible spectrum. This relation ultimately leads to the combination of an AR of 2–4 with a $x_{span} \sim 500-2000$ nm being optimal for solar absorption in nickel. It also explains the concave relation between FOM and AR observed in all of the samples shown in Figure 3(a). Increasing the aspect ratio beyond 2-4 for nickel reduces the FOM as it increases the IR emissivity and thereby the thermal emission. The increase in solar absorption and thermal emission with aspect ratio – as observed in Figure 3(a) and in the local minima presented in the results section can be attributed to subwavelength structure behavior when the spacing of the array is smaller than the incident wavelength [49]. Additionally, increasing a metallic ARGs aspect ratio (depth/period) has been previously shown to slightly increase the broadband emissivity of metal structures, including nickel [53, 54] and our results demonstrate this behavior.

Although periodic microstructures significantly enhance the spectral absorption of metals in the VIS/NIR, and therefore become excellent solar absorbing materials, metallic micropyramids cannot provide optimal passive cooling purely as a function of geometry. Unlike nickel and other metals, the complex refractive index of most ceramic and polymer materials is significantly lower and does not follow the same increasing trend as the wavelength increases that conductive materials such as nickel demonstrate. Subsequently, these materials are already well suited for absorption in particular wavelengths. By utilizing a similar combined effect between the complex refractive index and texture geometry, we can enable the anti-reflective behavior observed in both the alumina [55] and PDMS textures shown in the results. For both alumina and PDMS, the absorption bands are situated in the MIR/IR portion of the spectrum, with low ($k \sim 0$) extinction coefficients in the VIS/NIR bands leading to near 100% transmission of VIS/NIR radiation from wavelengths below ~ 6 µm. The absorption bands in the IR - attributed to an increase in the extinction coefficient (k) - enable IR anti-reflective behavior to be induced by geometry and further enhance emission characteristics of these materials. While the reflection is already low for these materials, optimized texturing can reduce the reflectivity to a value near 0. This relation can be observed in Figure 6(e), where an optimized texture expands the emission properties of alumina by making it emissive from 8 to 16 µm as a result of anti-reflective behavior. We validate the results shown in Figure 6(e) utilizing both an MG approximation in conjunction with a characteristic matrix [49, 56] and Rigorous-Coupled Wave Analysis (RCWA) [57, 58] in the Supplementary materials. The numerous assumptions in analytical and semi-analytical optical models limits their applicability across the geometric design space we present in this work. Classical, analytical, and semi-analytical models capture the anti-reflective behavior of micropryamid



designs [1] [2, 49, 56-59], but to ensure accurate optical and thus thermal computations across the entire design space we rely on the proven accuracy of FDTD simulations [60]

Fundamentally, the anti-reflective behavior of the alumina/PDMS textures is the same behavior observed in nickel, but the spectral region has shifted. A key difference between the polymer/ceramic optimization and the nickel optimization is the relation between the AR and x_{span}. Whereas Figure 3(a) makes it clear that the FOM of textured nickel depends strongly on AR as all of the x_{span} base dimensions demonstrate the same concave behavior with the inflection point near AR ~ 2-4; however, this behavior is not observed in alumina/PDMS. Figure 5(a) and Figure 7(a) show that the FOM instead behaves not only asymptotically but that the asymptote is reached far more quickly as x_{span} increases. Additionally, Figure 5(a) makes it clear that increasing the aspect ratio does not have as significant of an effect on the optical properties when the base dimension is significantly smaller than the critical incident wavelengths where anti-reflective behavior is observed. Alumina and PDMS have similar behavior between AR and FOM, but the "most optimal" geometric combinations for either material occur in different regions of the contour plots of Figure 5(b) and Figure 7(b). PDMS is the most optimal when $x_{span} > 15 \mu m$, and alumina texturing is most optimal when $x_{span} \sim 7.5-10 \mu m$. Unlike nickel, which has a distinct observed optimality region highlighted in the dark-red region in Figure 3(b), the saturation of the IR-emissivity for alumina/PDMS makes it difficult to define a the boundaries of the optimal geometric region. While we expect that increasing the bounds of our optimization process from an x_{span}/z_{span} of 15 $\mu m/20$ μm , respectively, to much larger values would enable the definition of a distinct optimal combination region akin to the nickel results in Figure 3(b), the computational time is not deemed to be worth the potential < 0.1-1% increase in emissivity. Additionally, it should be noted that as a consequence of the asymptotic behavior between the cooling FOM and AR, the alumina/PDMS optimization process very quickly yields highly optimal geometric solutions. For all the materials presented, while we can identify specific combinations of geometry that are most-optimal, we observe that local minimums in the cost-function can have significant variation in their aspect ratio despite marginal variation in the computed absorption/ emission efficiencies. The optimality region that develops in the thermal cost function is a result of the overlap between material properties, incident wavelength, and geometry. In simulating micropyramids made of other materials, we expect this trend to continue and that a micropyramid with an aspect ratio from 2 to 4 that has a base dimension near the critical wavelength with an appropriate complex refractive index ratio compared to the surrounding medium will yield effective anti-reflective behavior.

The optimized geometries for the heating and cooling cases (nickel and alumina/PDMS, respectively,) have a significant impact on the thermal performance of each material. In a typical ambient environment, Nickels best computed geometry ($x_{span} = 0.65 \mu m$ and $z_{span} = 2.1 \mu m$) has a surface temperature that is 44.2°C higher than an untextured nickel surface. This demonstrates the heating applications of textured nickel, as the textured nickel surface absorbs over 98.6% – 982 W/m² ⁻ of the incident solar radiation from $\lambda = 300$ nm to 2500 nm while the untextured surface only absorbs 33.7%. For cooling applications, textured alumina emits an average of 170 W/m² compared to the 106 W/m² figure of untextured alumina (emission from $\lambda = 8$ to 14 µm) under typical ambient conditions. This emission difference corresponds to a textured alumina surface temperature that is 9.8°C below the ambient and a surface temperature of 6.1°C below the ambient for the untextured case. Optimized PDMS geometry leads to the emission in the atmospheric transmission window of 8-14 µm increasing from 160 W/m² to 172.46 W/m² at a surface temperature of 300 K. While the 7.2% enhancement in textured PDMS's emission vs flat PDMS is not a significant as the geometrically induced absorption enhancement in nickel or emission increase in alumina (192.8% and 39.2%, respectively,) it is significant as it is only 0.007 W from the maximum blackbody emission from a surface at 300 K (over 99.99% of the theoretical limit). The emission spectra of the flat and textured PDMS relative to the blackbody limit is plotted in Supplementary Figure 7.

Conclusion

Using a minimization algorithm in conjunction with finite-difference time domain simulations, we have demonstrated that we can quickly arrive at micropyramid geometric parameters that provide near-ideal

solutions for thermal radiation and absorption. We have shown how we can rapidly optimize a two-variable geometric optical pattern to selectively reduce spectral reflection in metal, ceramic, and polymer materials. Further, we have shown that uncoated nickel periodic structures can research absorption efficiencies exceeding 98%, with our optimized design increasing emission from 337 W/m² (untextured) to 982 W/m². Simultaneously, the optimized nickel micropryamid design maintains a thermal emission that is below 20% of the maximum blackbody emission. By applying the same algorithmic process and geometry to both polymer and ceramic materials, we have shown how these materials can be designed to be more efficient thermal emitters. We have provided geometries that significantly improve the cooling performance of Alumina and PDMS surfaces from their untextured values of 106 W/m² and 160 W/m² to 170 W/m² and 172.4 W/m² – respectively – when the texture is applied. The enhancement of the thermal absorption in nickel and thermal emission in alumina and PDMS are driven by localized resonance and field confinement by the surface, and we have specified design guidelines on how to maximize these effects for the given materials. This work not only establishes the design criteria for micropyramids in thermal design applications, but it also delivers an easy to use algorithm, set of heat-transfer metrics, and adaptable framework that can be applied to a wide variety of future simulations and geometries.

Acknowledgments

This work was funded by the Aeronautics Research Mission Directorate (ARMD) of the National Aeronautics and Space Administration (NASA) through the NASA Fellowship Activity, under contract 80NSSC19K1671. Dr. Vikram Shyam from NASA's John H. Glenn Research Center is the technical advisor for this contract. Z.Y. and J.L. also thank the support provided by the National Science Foundation (No. ECCS-1807825 and ECCS-1935843).

ORCID

Jaeho Lee http://orcid.org/0000-0002-2207-4399

References

- [1] P. Campbell and M. A. Green, "Light trapping properties of pyramidally textured surfaces," *J. Appl. Phys.*, vol. 62, no. 1, pp. 243–249, 1987. DOI: 10.1063/1.339189.
- [2] A. Deinega, I. Valuev, B. Potapkin, and Y. Lozovik, "Minimizing light reflection from dielectric textured surfaces," *J. Opt. Soc. Am. A*, vol. 28, no. 5, pp. 770, 2011. DOI: 10.1364/josaa.28.000770.
- [3] T. Zhang, et al., "Black silicon with self-cleaning surface prepared by wetting processes," Nanoscale Res. Lett., vol. 8, no. 1, pp. 1–5, 2013. DOI: 10.1186/1556-276X-8-351.
- [4] Y. Liu, et al., "Hierarchical robust textured structures for large scale self-cleaning black silicon solar cells," Nano Energy, vol. 3, pp. 127–133, 2014. DOI:10.1016/j.nanoen.2013.11.002.
- [5] D. Z. Dimitrov and C. H. Du, "Crystalline silicon solar cells with micro/nano texture," *Appl. Surf. Sci.*, vol. 266, pp. 1–4, 2013. DOI:10.1016/j.apsusc.2012.10.081.
- [6] A. Peter Amalathas and M. M. Alkaisi, "Efficient light trapping nanopyramid structures for solar cells patterned using UV nanoimprint lithography," *Mater. Sci. Semicond. Process.*, vol. 57, pp. 54–58, October 2016, 2017, DOI:10.1016/j.mssp.2016.09.032.
- [7] A. Mavrokefalos, S. E. Han, S. Yerci, M. S. Branham, and G. Chen, "Efficient light trapping in inverted nanopyramid thin crystalline silicon membranes for solar cell applications," *Nano Lett.*, vol. 12, no. 6, pp. 2792–2796, 2012. DOI: 10.1021/nl2045777.
- [8] J. Zhu et al., "Optical absorption enhancement in amorphous silicon nanowire and nanocone arrays," Nano Lett., vol. 9, no. 1, pp. 279–282, 2009. DOI: 10.1021/nl802886y.
- [9] T. Rahman, M. Navarro-Cía, and K. Fobelets, "High density micro-pyramids with silicon nanowire array for photovoltaic applications," *Nanotechnology*, vol. 25, no. 48, pp. 485202, 2014. DOI: 10.1088/0957-4484/25/48/ 485202.
- [10] Y. Liu et al., "Hybridizing ZnO nanowires with micropyramid silicon wafers as superhydrophobic high-efficiency solar cells," Adv. Energy Mater., vol. 2, no. 1, pp. 47–51, 2012. DOI: 10.1002/aenm.201100287.
- [11] B. D. Choudhury, A. Abedin, A. Dev, R. Sanatinia, and S. Anand, "Silicon micro-structure and ZnO nanowire hierarchical assortments for light management," *Opt. Mater. Express*, vol. 3, no. 8, pp. 1039, 2013. DOI: 10.1364/ome.3.001039.



- [12] W. R. Wei et al., "Above-11%-efficiency organic-inorganic hybrid solar cells with omnidirectional harvesting characteristics by employing hierarchical photon-trapping structures," Nano Lett., vol. 13, no. 8, pp. 3658–3663, 2013. DOI: 10.1021/nl401540h.
- [13] P. Li et al., "Large-Scale nanophotonic solar selective absorbers for high-efficiency solar thermal energy conversion," Adv. Mater., vol. 27, no. 31, pp. 4585-4591, 2015. DOI: 10.1002/adma.201501686.
- [14] Y. J. Peng, H. X. Huang, and H. Xie, "Rapid fabrication of antireflective pyramid structure on polystyrene film used as protective layer of solar cell," *Sol. Energy Mater. Sol. Cells*, vol. 171, no. May, pp. 98–105, 2017. DOI: 10.1016/j.solmat.2017.06.013.
- [15] H. Sai, H. Yugami, Y. Kanamori, and K. Hane, "Solar selective absorbers based on two-dimensional W surface gratings with submicron periods for high-temperature photothermal conversion," Sol. Energy Mater. Sol. Cells, vol. 79, no. 1, pp. 35-49, 2003. DOI: 10.1016/S0927-0248(02)00364-1.
- [16] H. Zhang et al., "Biologically inspired flexible photonic films for efficient passive radiative cooling," Proc. Natl. Acad. Sci., vol. 117, no. 26, pp. 202001802, 2020. DOI: 10.1073/pnas.2001802117.
- [17] P. Nagpal, N. C. Lindquist, S. H. Oh, and D. J. Norris, "Ultrasmooth patterned metals for plasmonics and metamaterials," Science (80-.), vol. 325, no. 5940, pp. 594-597, 2009. DOI: 10.1126/science.1174655
- [18] J. H. Park, et al., "Fabrication of smooth patterned structures of refractory metals, semiconductors, and oxides via template stripping," ACS Appl. Mater. Interfaces, vol. 5, no. 19, pp. 9701-9708, 2013. DOI: 10.1021/am402756d.
- [19] H. Lu and C. Gang, "Analysis of optical absorption in silicon nanowire arrays for photovoltaic applications," Nano Lett., vol. 7, no. 11, pp. 3249-3252, 2007. DOI: 10.1021/nl071018b.
- [20] A. R. Zanatta, "Revisiting the optical bandgap of semiconductors and the proposal of a unified methodology to its determination," Sci. Rep., vol. 9, no. 1, pp. 11225, 2019. DOI: 10.1038/s41598-019-47670-y.
- [21] P. Singh et al., "Fabrication of vertical silicon nanowire arrays on three-dimensional micro-pyramid-based silicon substrate," J. Mater. Sci., vol. 50, no. 20, pp. 6631-6641, 2015. DOI: 10.1007/s10853-015-9210-y.
- S. Ge et al., "Design and preparation of a micro-pyramid structured thin film for broadband infrared antireflection," Coatings, vol. 8, no. 5, pp. 192, 2018. DOI: 10.3390/coatings8050192.
- [23] H. Sai, H. Yugami, Y. Akiyama, Y. Kanamori, and K. Hane, "Spectral control of thermal emission by periodic microstructured surfaces in the near-infrared region," J. Opt. Soc. Am. A, vol. 18, no. 7, pp. 1471, 2001. DOI: 10.1364/josaa.18.001471.
- [24] Y. Nishijima, et al., "Anti-reflective surfaces: cascading nano/microstructuring," APL Photonics, vol. 1, no. 7, pp. 076104, 2016. DOI: 10.1063/1.4964851.
- [25] D. Wu et al., "The design of ultra-broadband selective near-perfect absorber based on photonic structures to achieve near-ideal daytime radiative cooling," Mater. Des., vol. 139, pp. 104-111, 2018. DOI: 10.1016/j. matdes.2017.10.077.
- [26] J. Zhu, C. M. Hsu, Z. Yu, S. Fan, and Y. Cui, "Nanodome solar cells with efficient light management and self-cleaning," Nano Lett., vol. 10, no. 6, pp. 1979–1984, 2010. DOI: 10.1021/nl9034237.
- [27] R. Kumar and M. A. Rosen, "Thermal performance of integrated collector storage solar water heater with corrugated absorber surface," Appl. Therm. Eng., vol. 30, no. 13, pp. 1764-1768, 2010. DOI: 10.1016/j. applthermaleng.2010.04.007.
- [28] L. Zhou, X. Yu, and J. Zhu, "Metal-core/semiconductor-shell nanocones for broadband solar absorption enhancement," Nano Lett., vol. 14, no. 2, pp. 1093-1098, 2014. DOI: 10.1021/nl500008y.
- [29] B. J. Lee, Y. Bin Chen, S. Han, F. C. Chiu, and H. J. Lee, "Wavelength-selective solar thermal absorber with two-dimensional nickel gratings," J. Heat Transfer, vol. 136, no. 7, pp. 1-7, 2014. DOI: 10.1115/1.4026954.
- X. Yin, R. Yang, G. Tan, and S. Fan, "Terrestrial radiative cooling: using the cold universe as a renewable and sustainable energy source," Science (80-.), vol. 370, no. 6518, pp. 786-791, 2020. DOI: 10.1126/science.abb0971.
- [31] A. Krishna, et al., "Ultraviolet to mid-infrared emissivity control by mechanically reconfigurable graphene," Nano Lett., vol. 19, no. 8, pp. 5086–5092, 2019. DOI: 10.1021/acs.nanolett.9b01358.
- [32] M. Sala-Casanovas, A. Krishna, Z. Yu, and J. Lee, "Bio-Inspired stretchable selective emitters based on corrugated Nickel for personal thermal management," Nanoscale Microscale Thermophys. Eng., vol. 23, no. 3, pp. 173-187, 2019. DOI: 10.1080/15567265.2019.1586017.
- [33] A. P. Raman, M. A. Anoma, L. Zhu, E. Rephaeli, and S. Fan, "Passive radiative cooling below ambient air temperature under direct sunlight," Nature, vol. 515, no. 7528, pp. 540-544, 2014. DOI: 10.1038/nature13883.
- Y. Zhai et al., "Scalable-manufactured randomized glass-polymer hybrid metamaterial for daytime radiative cooling," Science (80-.), vol. 355, no. 6329, pp. 1062-1066, 2017. DOI: 10.1126/science.aai7899.
- [35] J. Mandal et al., "Hierarchically porous polymer coatings for highly efficient passive daytime radiative cooling," Science (80-.), vol. 362, no. 6412, pp. 315–319, 2018. DOI: 10.1126/science.aat9513.
- [36] J. J. D. Leon, A. M. Hiszpanski, T. C. Bond, and J. D. Kuntz, "Design rules for tailoring antireflection properties of hierarchical optical structures," Adv. Opt. Mater., vol. 5, no. 13, pp. 1-8, 2017. DOI: 10.1002/adom.201700080.
- [37] J. Seo et al., "Design of a broadband solar thermal absorber using a deep neural network and experimental demonstration of its performance," Sci. Rep., vol. 9, no. 1, pp. 1-9, 2019. DOI: 10.1038/s41598-019-51407-2.
- S. Haghanifar, et al., "Discovering high-performance broadband and broad angle antireflection surfaces by machine learning," Optica, vol. 7, no. 7, pp.784, 2020. DOI: 10.1364/OPTICA.387938.

- [39] M. Elzouka, C. Yang, A. Albert, R. S. Prasher, and S. D. Lubner, "Interpretable forward and inverse design of particle spectral emissivity using common machine-learning models," *Cell Reports Phys. Sci.*, vol. 1, no. 12, pp. 100259, 2020. DOI: 10.1016/j.xcrp.2020.100259.
- [40] X. Nie, et al., "Cool white polymer coatings based on glass bubbles for buildings," Sci. Rep., vol. 10, no. 1, pp. 1–10, 2020. DOI: 10.1038/s41598-020-63027-2.
- [41] Z. Yu, X. Nie, A. Yuksel, and J. Lee, "Reflectivity of solid and hollow microsphere composites and the effects of uniform and varying diameters," *J. Appl. Phys.*, vol. 128, no. 5, pp. 053103, 2020. DOI: 10.1063/5.0015650.
- [42] H. Wang and L. Wang, "Perfect selective metamaterial solar absorbers," *Opt. Express*, vol. 21, no. S6, pp. A1078, 2013. DOI: 10.1364/oe.21.0a1078.
- [43] D. L. C. Chan, M. Soljačić, and J. D. Joannopoulos, "Thermal emission and design in one-dimensional periodic metallic photonic crystal slabs," *Phys. Rev. E - Stat. Nonlinear Soft Matter Phys.*, vol. 74, no. 1, pp. 206–214, 2006. DOI: 10.1103/PhysRevE.74.016609.
- [44] R. H. Byrd, J. C. Gilbert, and J. Nocedal, "A trust region method based on interior point techniques for nonlinear programming," *Math. Program. Ser. B*, vol. 89, no. 1, pp. 149–185, 2000. DOI: 10.1007/PL00011391.
- [45] R. Poli, J. Kennedy, and T. Blackwell, "Particle swarm optimization an overview," pp. 33–57, 2007. DOI: 10.1007/ s11721-007-0002-0.
- [46] D. Whitley, "A genetic algorithm tutorial," 1994.
- [47] M. Planck, The Theory of Heat Radiation. Philidelphia, PA: P. Blakinston's Son & Co., 1914.
- [48] A. Srinivasan, B. Czapla, J. Mayo, and A. Narayanaswamy, "Infrared dielectric function of polydimethylsiloxane and selective emission behavior," *Appl. Phys. Lett.*, vol. 109, no. 6, pp. 061905, 2016. DOI: 10.1063/1.4961051.
- [49] S. Chattopadhyay, et al., "Anti-reflecting and photonic nanostructures," Mater. Sci. Eng. R Rep., vol. 69, no. 1–3, Elsevier Ltd, pp. 1–35, Jun 20, 2010. DOI: 10.1016/j.mser.2010.04.001.
- [50] J. C. Garnett, Philos. Trans. R. Soc. A Math. Phys. Eng. Sci., vol. 203, pp. 385, 1904.
- [51] J. C. M. Garnett, Philos. Trans. R. Soc. A Math. Phys. Eng. Sci., vol. 205, pp. 237, 1906.
- [52] D. A. G. Bruggeman Von, "Berechnzerrg verschCedener physikalducher Eonstanten von heterogenew Yuhstan. xen 1," Ann. Phys., 1935.
- [53] R. T. Kivaisi and L. Stensland, "Spectral selectivity of nickel and chromium rough surfaces," Appl. Phys. A Solids Surfaces, vol. 27, no. 4, pp. 233–238, 1982. DOI: 10.1007/BF00619084.
- [54] H. G. Craighead, R. E. Howard, and D. M. Tennant, "Selectively emissive refractory metal surfaces," Appl. Phys. Lett., vol. 38, no. 2, pp. 74–76, 1981. DOI: 10.1063/1.92253.
- [55] E. D. Palik, Handbook of Optical Constants of Solids. Orlando: Academic Press, 1985.
- [56] H. A. Macleod, Thin-Film Optical Filters. 1986.
- [57] M. G. Moharam and T. K. Gaylord, "Rigorous coupled-wave analysis of planar-grating diffraction," vol. 71, no. 7, pp. 1981.
- [58] M. G. Moharam and T. K. Gaylord, "Diffraction analysis of dielectric surface-relief gratings," J. Opt. Soc. Am., vol. 72, no. 10, pp. 1385–1392, 1982. DOI: 10.1364/JOSA.72.001385.
- [59] K. E. Torrance and E. M. Sparrow, "Theory for off-specular reflection from roughened surfaces*," J. Opt. Soc. Am., vol. 57, no. 9, pp. 1105, 1967. DOI: 10.1364/josa.57.001105.
- [60] K. Han and C. Chang, "Numerical modeling of sub-wavelength anti-reflective structures for solar module applications," pp. 87–128, 2014. DOI: 10.3390/nano4010087.

Preflight Results

Document Information

Preflight Information

Title: Optical Analysis and Optimization of Micropyramid Textoffile: for TheonaleRadianological Analysis and Optimization of Micropyramid Textoffile:

Author: Version: Qoppa jPDFPreflight v2021R1.00

Creator: Arbortext Advanced Print Publisher 11.0.3433/W UniDatte May 26, 2022 5:14:52 PM

Producer: PDFlib+PDI 9.0.3p4 (C++/Win32)

Legend: (X) - Can NOT be fixed by PDF/A-1b conversion.

(!X) - Could be fixed by PDF/A-1b conversion. User chose to be warned in PDF/A settings.

Page 4 Results

(X) Font widths must be the same in both the font dictionary and the embedded font file.

(X) Font widths must be the same in both the font dictionary and the embedded font file.

Page 5 Results

(X) Font widths must be the same in both the font dictionary and the embedded font file.

(X) Font widths must be the same in both the font dictionary and the embedded font file.

Page 6 Results

- (X) Font widths must be the same in both the font dictionary and the embedded font file.
- (X) Font widths must be the same in both the font dictionary and the embedded font file.
- (X) Font widths must be the same in both the font dictionary and the embedded font file.
- (X) Font widths must be the same in both the font dictionary and the embedded font file.

Page 7 Results

(X) Font widths must be the same in both the font dictionary and the embedded font file.